SUPPLEMENTAL MATERIAL

A. Experimental Videos

High-speed videos for droplets A-D presented in Fig. 4 are included as Supplemental Material. Each movie has been slowed down 200 times (i.e. captured at 2000 fps and played back at 10 fps).

B. Comparison of Dimensionless Numbers

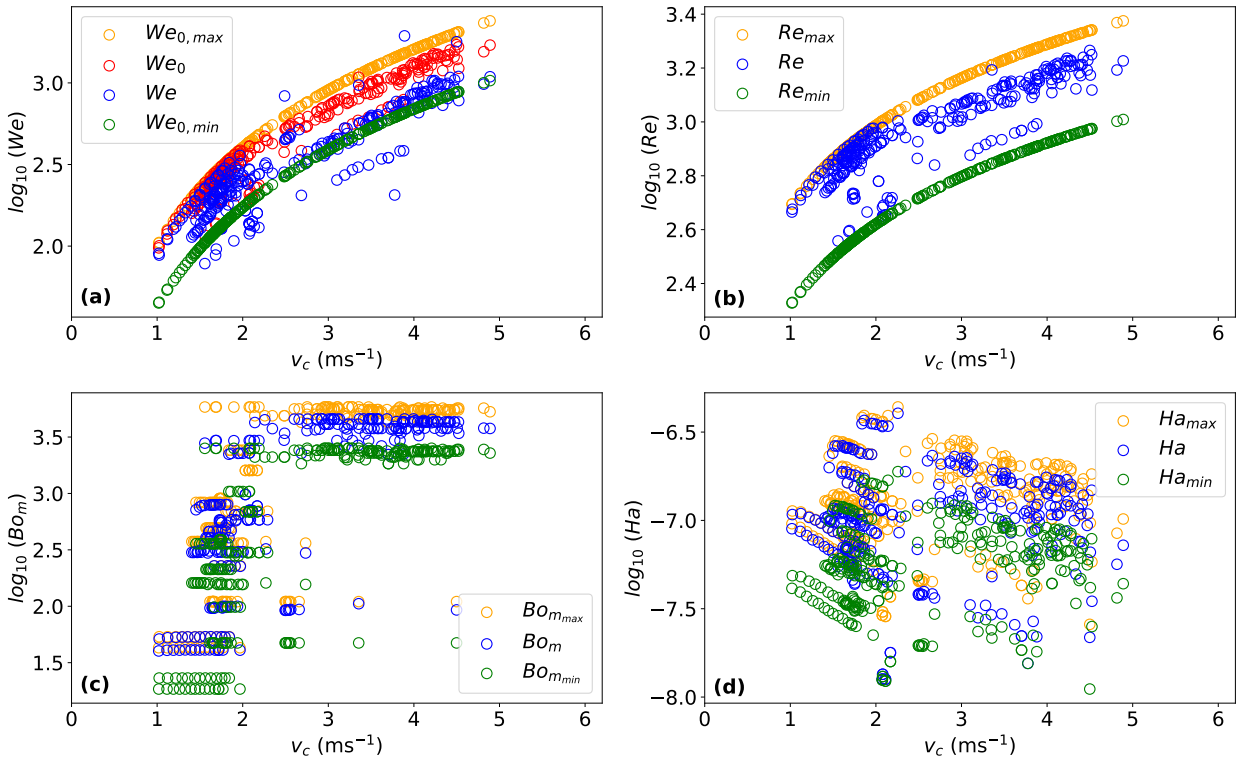

FIG. S1. Plots of the dimensionless numbers (a) We and We_0, (b) Re, (c) Bo_m, and (d) Ha as a function of center-of-mass velocity prior to impact. Each plot shows the calculations for each experiment using the three different diameters D_{max}, D_0, and D_{min} as a length scale.

A comparison of dimensionless numbers as a function of the centre-of-mass velocity of droplets prior to impact (v_c) is presented in Fig. S1. For each of the dimensionless numbers We_0, Re, Bo_m and Ha, values were calculated for each droplet using the equivalent volume D_0, as well as bounding values using the smallest (D_{min}) and largest (D_{max}) equivalent

diameters from the data set.

The main dimensionless number used in this work, i.e. values of We from equation (2), are included in Fig. S1(a). The difference between We and We_0 is caused by drop elongation. Each of We, We_0 and Re are near-monotonic with respect to v_c, although not entirely so due to variable drop size and shape at impact (captured by these numbers). In contrast, Bo_m and Ha are clearly non-monotonic because the impact velocity depends on the applied field.

C. Measurement of Contact Line Width

During the initial spread of the droplets, the contact angle is greater than 90°, so that it is of interest to measure the contact line width as shown in Fig. S2(a) as well as the drop diameter (i.e. the widest extent of the droplet). The contact line is identified using the clearly visible reflection of the droplet from the glass slide. From a thresholded image of the spreading droplet, a search for concavity on either side (Figure S2(b)) can be used to identify the edge of the contact line. For analysis, the contact line is defined by a straight line fit through the edge points found on either side of the droplet in 5 different frames. The diameter is similarly found using the central point of concavity at the droplet edge.

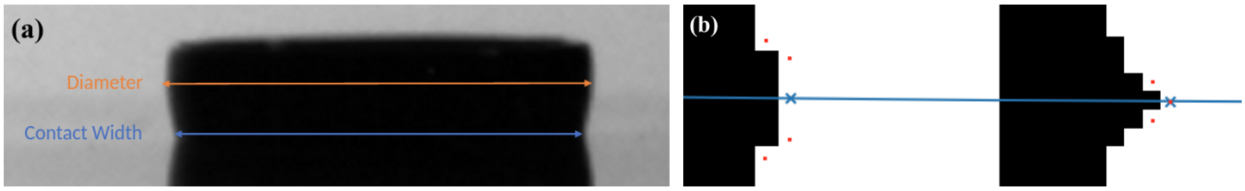

FIG. S2. Image analysis for measurement of the contact line width. (a) Image of a ferrofluid drop spreading on a glass slide, with the diameter and contact line width labelled. (b) Magnified image of the left side of a droplet in two different frames (left and right). Individual pixels are visible, and a threshold has been applied so that white pixels represent the imaged droplet, and black pixels represent the background. Red dots define the identified concave contour, the blue crosses indicate contact points, and the blue line is the contact line.

D. Maximum Spreading Diameter

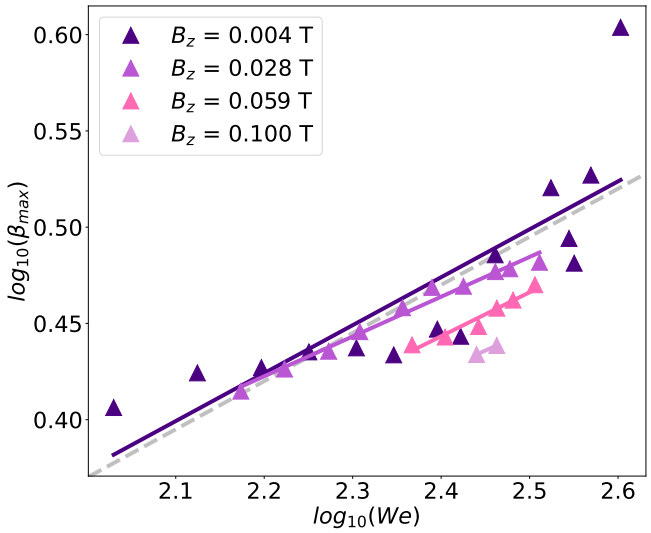

FIG. S3. Log-log plot of maximum spread factor as a function of We for a subset of the ferrofluid drop impact experiments with similar droplet size. Solid lines are linear fits to each data set, and the dashed grey line has a gradient of 0.25.

Figure S3 shows the relation between the normalized maximum spreading diameter, the impact Weber number, and the B-field for experiments conducted at relatively low B_z. Low B_z data are appropriate to use because the initial spread of the droplet can be distinguished from more long-term rebound or growth of the spreading diameter. Furthermore, for these data the average volume of the droplets was reasonably constant at 7.29 ± 0.14 μl.

As expected, the maximum spread generally increases with We for any particular magnet position. With increasing B-field, the maximum spread generally decreases. This is consistent with the increased inwards radial force that the droplets experience for these B_z values (the fields considered here are not sufficient to cause rim formation, see Section IV D). Linear fits were calculated and plotted for data points at each value of B_z. For droplet impacts on solid surfaces, maximum spread is often observed to scale as $\beta_{\max} \propto \mathrm{We}^{0.25}$ [28]. The fits in Fig. S3 all have a gradient close to 0.25 (shown by the dashed grey line) although the data are limited and inconclusive in some places.

E. Classifications - Alternative Plots

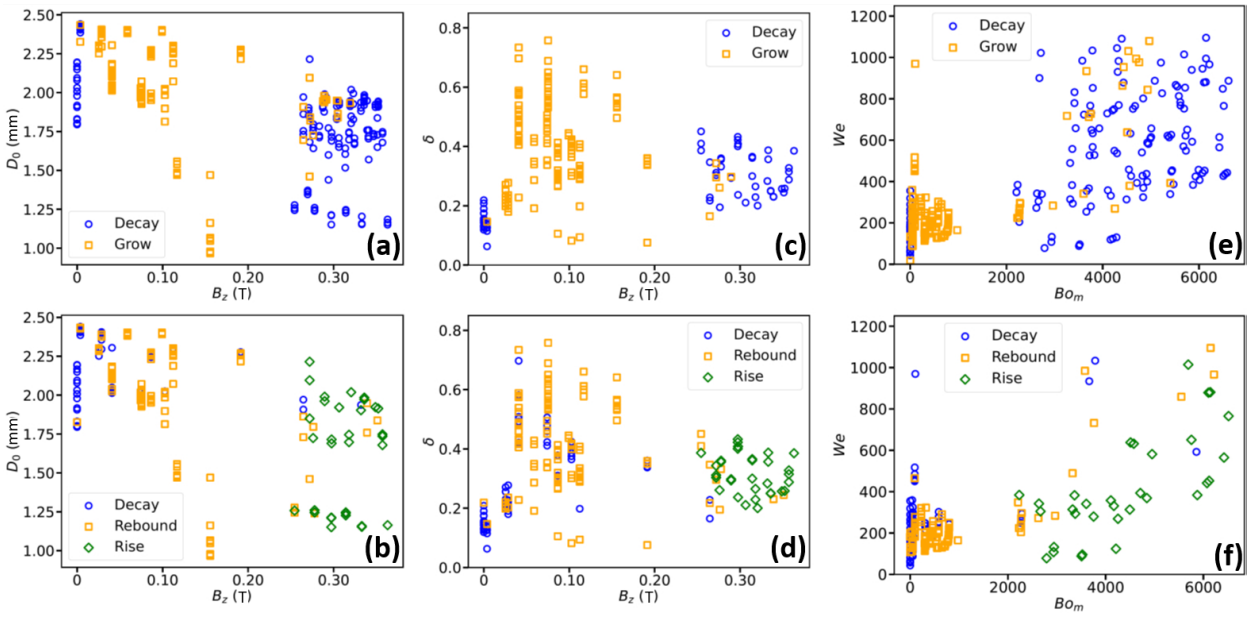

FIG. S4. Classifications of height (above - a, c, e) and contact line (below - b, d, f) dynamics for the experiments from Fig. 6 in the main text, plotted as a function of alternative parameters. Data points do not exactly correspond between plots if the imaging quality or analysis precluded a classification.

Figure S4 re-plots the data from Fig. 6 in the main text as a function of alternative experimental parameters. Plots with particular length scales on the vertical axis (Figs. S4(a)-(d)) do not explain the outcomes that are non-monotonic in B_z. Figures S4(e)-(f) use two dimensionless numbers, We and the magnetic Bond number Bo_m. The trend in the outcomes is less well defined for Bo_m than for B_z.

F. Rim Formation - Alternative Plots

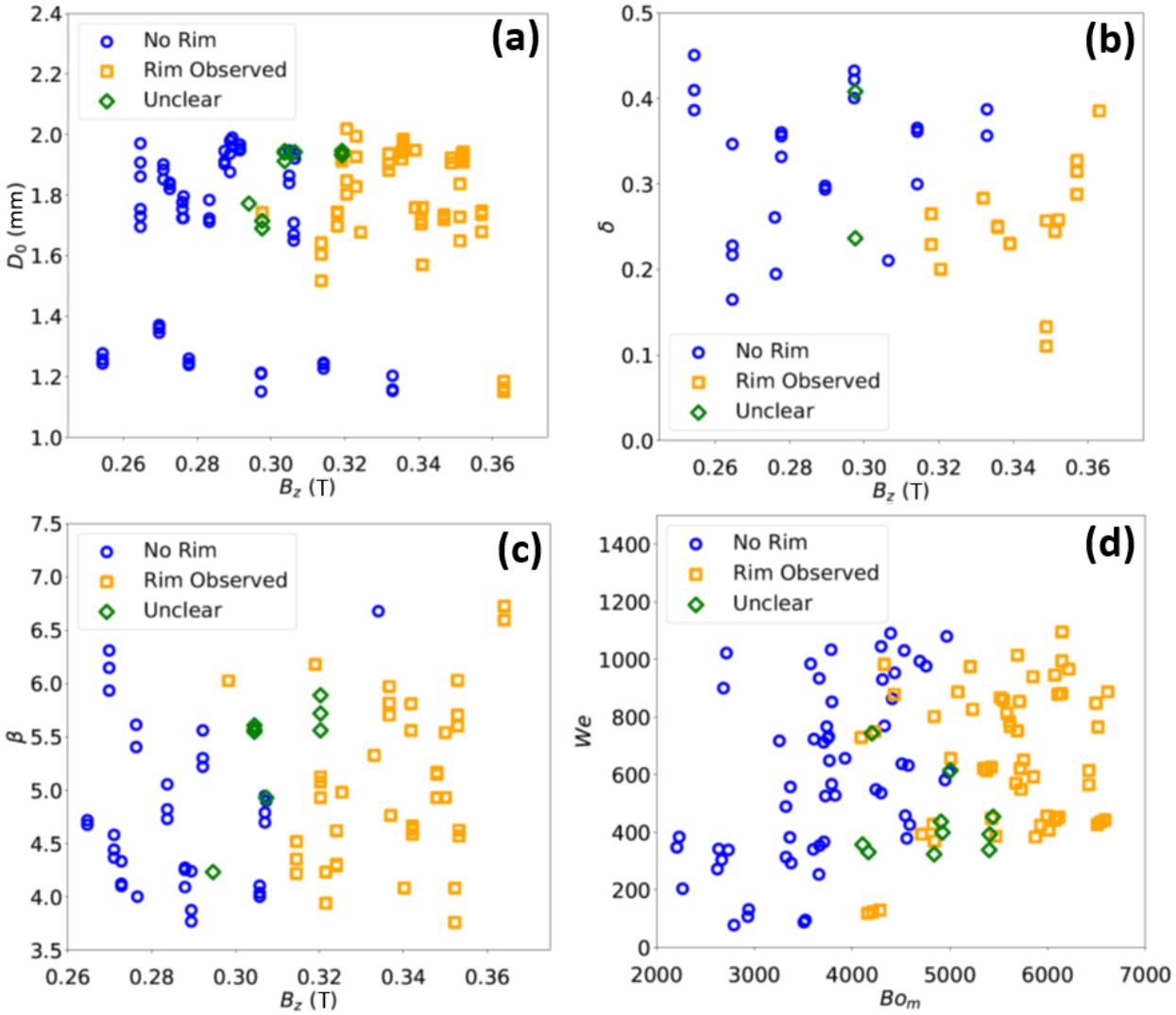

FIG. S5. Classifications of rim outcomes for the experiments from Fig. 9 in the main text, plotted as a function of alternative parameters. Data points do not exactly correspond between plots if the imaging quality or analysis precluded a classification.

Figure S5 re-plots the data from Fig. 9 in the main text as a function of alternative experimental parameters. Plots with particular length scales on the vertical axis (Figs. S4(a)-(c)) do not give improved understanding of the differences between outcomes. It is possible that the experiments for relatively small droplets near $0.32 \leq B_z \leq 0.34$ are correlated with 'no rim' outcomes. As in Fig. S4, the use of dimensionless numbers in Fig. S5(d) does not yield a clearer division between outcomes.

G. Rim Coalescence for Inner Peaks

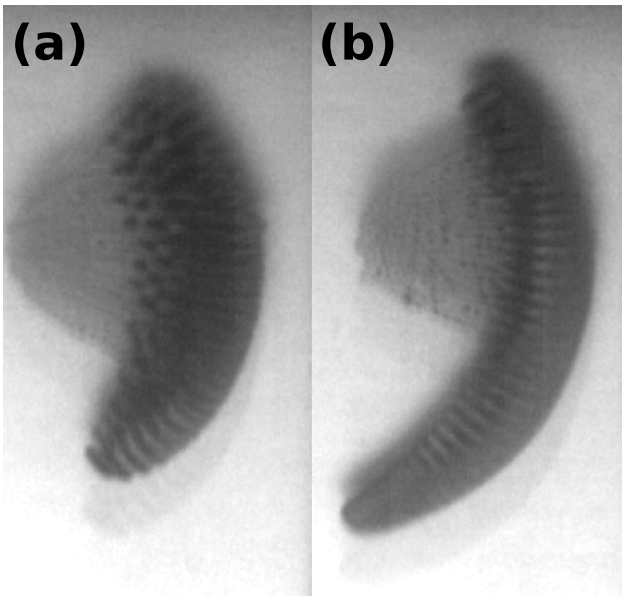

FIG. S6. Images of droplets at 37 s after impact producing slightly different rim morphologies. (a) $We = 393$, $V = 2.54$ μl, $v = 3.11$ m/s, $h_0 = 3.47$ mm, $B = 0.319$ T. (b) $We = 453$, $V = 2.79$ μl, $v = 3.23$ m/s, $h_0 = 2.26$ mm, $B = 0.358$ T.

Figure S6 shows two asymmetric rims formed after slightly off-centre impacts at relatively high magnetic field, pictured a long time after impact. In Fig. S6(a), peaks on the inner side of the rim have not coalesced with the rim, in contrast with Fig. S6(b). In the latter case, the magnetic flux density is higher, suggesting that a relatively high field is required to overcome peak repulsion and produce coalescence with the rim. Also note that the width of the rim is smaller when the field is greater.